

Supporting Information

Semiconductive MOF as a promising platform for green and efficient electromagnetic shielding

Congjie Chen^a, Zhen Shan^c, Xiangyu Gao^a, Bocong Li^a, Jiayue Li^a, Yuexia Dong^a, Jiawei Ma^a, Hongwei Yang^a, Jian Su^{a,} and Gen Zhang^{a,b,*}*

^a Key Laboratory for Soft Chemistry and Functional Materials of Ministry of Education, School of Chemistry and Chemical Engineering, Nanjing University of Science and Technology, Nanjing 210094, China

^b Key Laboratory of Preclinical Study for New Drugs of Gansu Province, Lanzhou University, Lanzhou 730000, China

^c State Key Laboratory of Metal-organic Chemistry, Shanghai Institute of Organic Chemistry, Chinese Academy of Sciences, Shanghai 200032, China

† C.C. and Z.S. contributed equally

**Corresponding author. E-mail: sujian@njjust.edu.cn; zhanggen@njjust.edu.cn*

Equation:

Among them, E, H, and P are the electric field strength, magnetic field strength, and EM wave power, respectively. Meanwhile, considering the mechanism of EM waves in materials, Schelkunoff's formula indicates that EMI SE_T is an important indicator of material attenuation ability, consisting of reflection loss, absorption loss, and multiple reflection loss.

$$SE_T(dB) = SE_A + SE_R + SE_M \quad (1)$$

$$SE_A(dB) = 8.7d\sqrt{\pi f\mu\sigma} \quad (2)$$

$$SE_R(dB) = 39.5 + 10 \log \sqrt{\frac{\sigma}{2\pi f\mu}} \quad (3)$$

Where d represents material thickness, f represents incident wave frequency, μ represents magnetic permeability, and σ represents electrical conductivity.

In experiments, EMI SE_T is usually determined by measuring scattering parameters S11 and S21 using a vector network analyzer (VNA), and their relationship is represented by the following equation:

$$SE_T(dB) = -10 \log \left(\frac{1}{|S_{21}|^2} \right) \quad (4)$$

$$R = |S_{11}|^2 \quad (5)$$

$$T = |S_{21}|^2 \quad (6)$$

$$g_s = \frac{1}{|S_{11}|^2} - \frac{|S_{21}|^2}{|S_{11}|^2} - 1 \quad (7)$$

$$A = 1 - |S_{11}|^2 - |S_{21}|^2 \quad (8)$$

$$R + A + T = 1 \quad (9)$$

$$A_{eff} = \frac{1-R-T}{1-R} \quad (10)$$

When electromagnetic waves encounter the surface of shielding materials, the sum of their reflection coefficient (R), absorption coefficient (A), and transmission coefficient (T) must be conserved. They can be calculated by scattering parameters and expressed as: $A_{eff} = (1-R-T)/(1-R)$

$$SE_R = -10 \log(1 - |S_{11}|^2) \quad (11)$$

$$SE_A = -10 \log\left(\frac{|S_{21}|^2}{1 - |S_{11}|^2}\right) \quad (12)$$

Materials

Thieno[3,2-*b*]thiophene (TT), (3,4-dimethoxyphenyl)boronic acid were purchased from Dipak Reagent Co., LTD (Shanghai, China), n-butyl alcohol, o-dichlorobenzene, Pd(PPh₃)₄, anhydrous K₂CO₃, Cu(CH₃COO)₂ were purchased from Energy Chemical (Shanghai, China). N, N-dimethylformamide (DMF), tetrahydrofuran (THF) were purchased from J&K Chemicals (Shanghai, China). All the commercial chemicals were directly used without further purification.

Synthesis of the secondary building unit (TBTT-8OH)

The entire synthesis process from thieno[3,2-*b*]thiophene (TT) to octahydroxyl tetraphenylthieno-[3,2-*b*]thiophene (TBTT-8OH) was synthesized according to our previous work ^[1].

Synthesis of the CuMOF-1D

In a 40 mL glass vial, TBTT-8OH (80 mg, 0.12 mmol) and Cu(OAc)₂ (49.6 mg, 0.24 mmol) were dispersed in EtOH/H₂O (v/v = 8.0 mL/8.0 mL) via ultrasonic treatment for a duration of 5 minutes, resulting in a charcoal grey suspension. The screwed vial with suspension was standing in an oven set at 85°C for 5 days. After cooling to room temperature, the precipitate was isolated by filtration and washed with deionized water and EtOH for three times, respectively. The synthetic product was collected and dried under vacuum at 100°C overnight, finally obtain the dark black powder.

Synthesis of the sql-CuMOF-2D

In a 40 mL glass vial, TBTT-8OH (80 mg, 0.12 mmol) and Cu(OAc)₂ (49.6 mg, 0.24 mmol) were dispersed in DMF/H₂O (v/v = 12.0 mL/4.0 mL) by ultrasonic treatment for 5 min to afford charcoal grey suspension. The screwed vial with suspension was placed in 85°C oven for 5 days. After cooling to room temperature, the precipitate was isolated by filtration and washed with deionized water and EtOH for three times, respectively. The product was collected and dried under vacuum as black powder.

Characterization

Powder X-ray diffraction (PXRD) patterns were collected on a Bruker D8 ADVANCE diffractometer using Cu K α radiation ($\lambda = 1.5418 \text{ \AA}$). Scanning electron microscope (SEM) images were collected using a Germany JZEISS Sigma 360 system. Transmission electron microscope (TEM) images were obtained with a Japan JEOL JEM-F200 system. Gas

adsorption: N₂ adsorption and desorption measurements were performed at 77 K using ASAP 2020, Micromeritics Instrument Corp, USA. Pore size distributions and pore volumes were derived from the adsorption isotherms. The MOFs were degassed at 60°C for 8 hours using an automatic volumetric adsorption apparatus. Thermogravimetric analysis (TGA): TGA was performed using a TGA/SDTA851E under flowing N₂ with 10 K/min ramp rate. Samples were heated in a Platinum pan (800°C, 10 °C/min) under a N₂ flux (60 mL/min). X-ray photoelectron spectroscopy (XPS): XPS was measured on a Thermo Scientific K-Alpha. Current density tester (2602B SYSTEM Source Meter) was used to research the electrical conductivity (EC) of samples.

Electromagnetic measurements

The electromagnetic parameters of all the samples were measured on a vector network analyzer (Agilent PNA N5224A) in transmission-reflection mode at 2–18 GHz. The different proportions MOFs were uniformly mixed with different proportions paraffin at room temperature and pressed into standard rings for the measurement of EMW shielding. The outer diameter, inner diameter and thickness of toroidal-like specimen were set to be 7.00, 3.04 and 3.00 mm, respectively. Paraffin has relatively low permittivity, which means that it is almost transparent to EMW. The microwave absorption properties of samples mixed with paraffin can be used to characterize the nature of materials.

Here is a supplement for the preparation process for pure MOF samples: Place the pure MOF sample into a coaxial ring mold, press it into a ring with a fixed pressure of 20mpa, then take out the sample and place it in the coaxial testing mold cavity. Conduct testing.

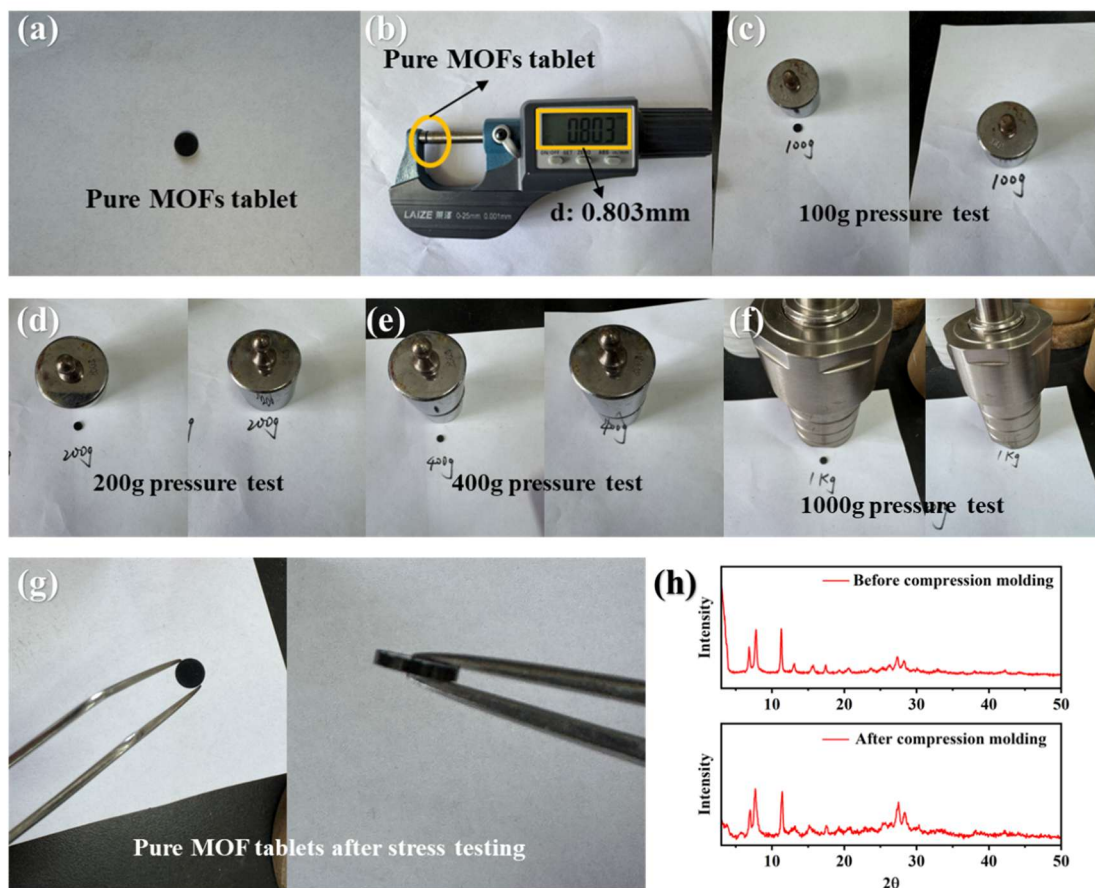


Fig. S1. Simple mechanical integrity testing of pure CuMOF-1D tablets.

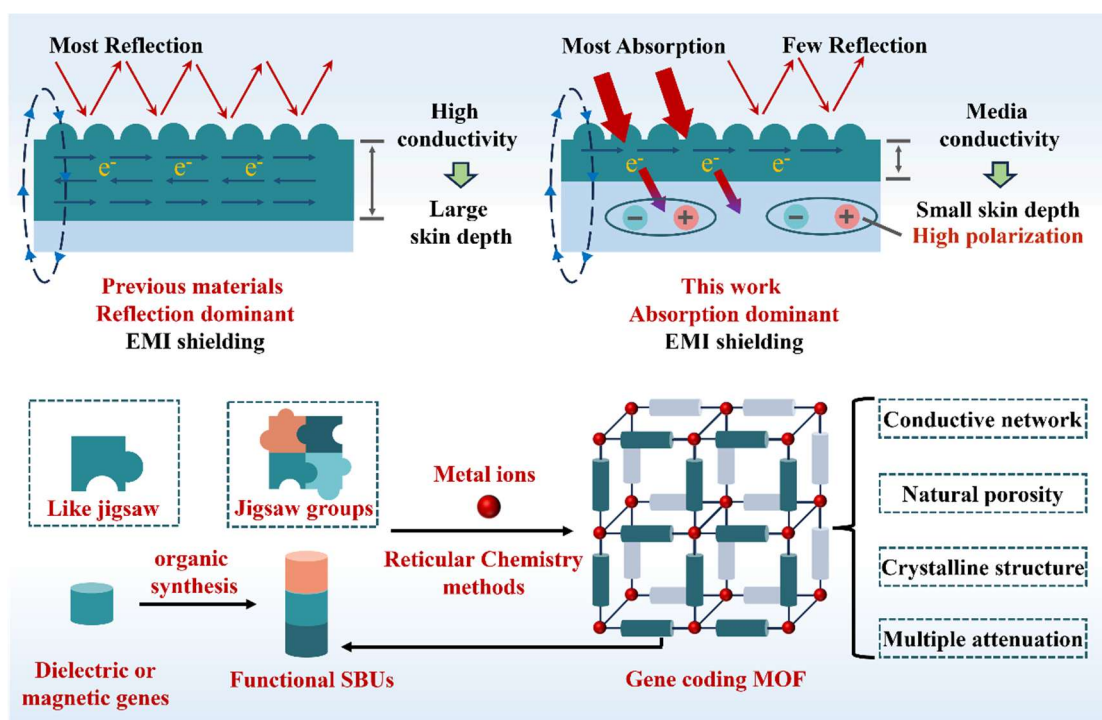
To verify the mechanical integrity of the pure MOF tablet, we pressed a pure CuMOF-1D tablet with a diameter of 5 mm and a thickness of 0.8 mm under the same pressure, as shown in Figures S1a and S1b. The mechanical integrity of the material was simply verified via pressure tests using weights of different masses (100 g, 200 g, 400 g,

1 kg), as illustrated in Figures S1c–f. After the tests, the sample showed almost no damage (Figure S1g). The PXRD patterns of the sample before and after tableting also confirmed that the sample was not destroyed during tableting or after experiencing different pressures (Figure S1h).

Theoretical calculation method:

We have employed the Vienna Ab Initio Package (VASP) [2] to perform all spin-polarized density functional theory (DFT) calculations within the generalized gradient approximation (GGA) using the Perdew-Burke-Ernzerhof (PBE) [3] formulation. We have chosen the projected augmented wave (PAW) potentials [4,5] to describe the ionic cores and take valence electrons into account using a plane wave basis set with a kinetic energy cutoff of 450 eV. Partial occupancies of the Kohn–Sham orbitals were allowed using the Gaussian smearing method and a width of 0.05 eV. The electronic energy was considered self-consistent when the energy change was smaller than 10^{-5} eV. A geometry optimization was considered convergent when the energy change was smaller than 0.02 eV \AA^{-1} . The weak interaction was described by DFT+D₃ method using empirical correction in Grimme’s scheme [6, 7]. The Dipole correction taken into account for this calculation. The equilibrium lattice constants of two MOF unit cells were optimized when a $1 \times 1 \times 6$ k-point grid in the Brillouin zone

was used for k-point sampling, and all atoms were allowed to relax.



Schem. 1. The difference of shielding mechanism between electromagnetic shielding materials dominated by reflection loss and electromagnetic shielding materials dominated by absorption loss, and the schematic diagram of MOF gene coding design strategy proposed in this work.



Fig. S2. Conjugated structure after ring-closure.

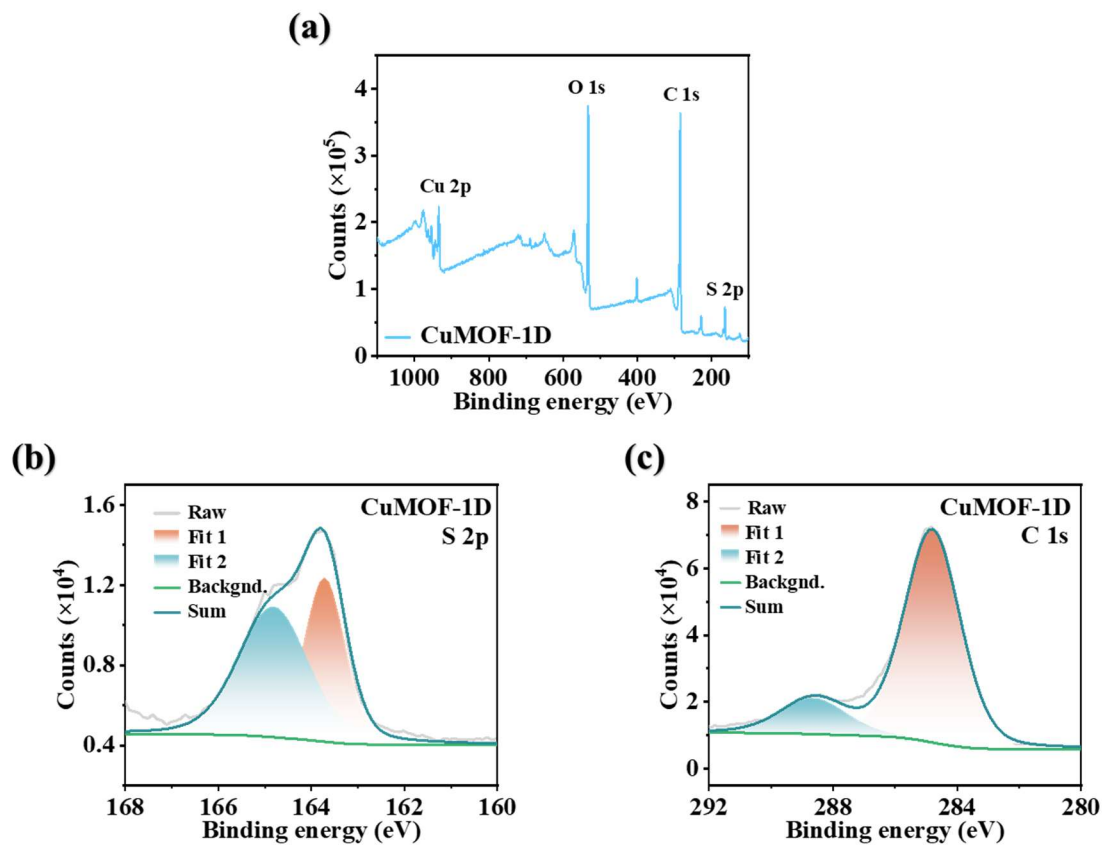


Fig. S3. (a) XPS analysis of full energy spectrum for CuMOF-1D; (b) XPS high resolution spectra of (b), S 2p region (c) C 1s region for CuMOF-1D.

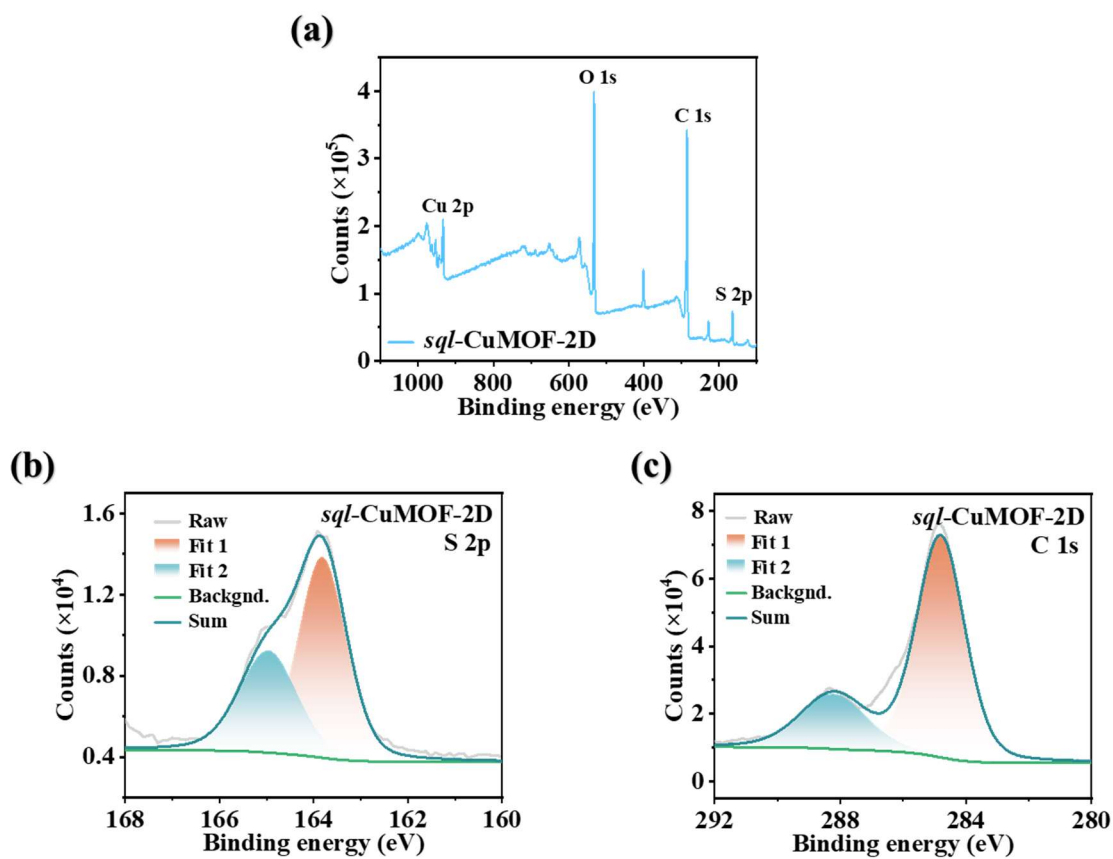


Fig. S4. (a) XPS analysis of full energy spectrum for *sql*-CuMOF-2D; (b) XPS high resolution spectra of (b), S 2p region (c) C1s region for *sql*-CuMOF-2D.

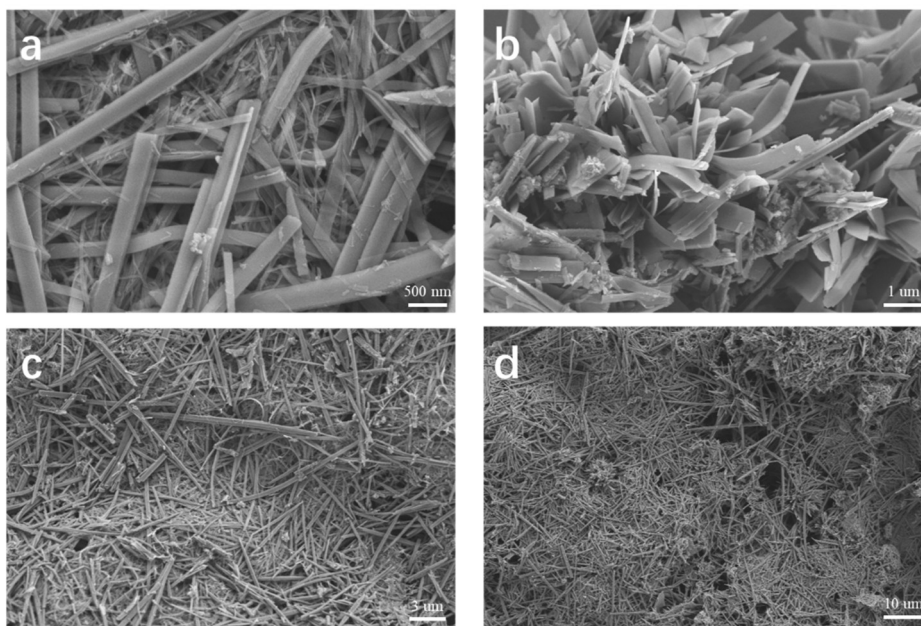


Fig. S5. The SEM images of CuMOF-1D.

Map Sum Spectrum					
Element	Line Type	Weight %	Weight % Sigma	Atomic %	
C	K series	53.11	0.20	72.03	
O	K series	17.12	0.13	17.44	
S	K series	11.54	0.07	5.86	
Cu	L series	18.23	0.12	4.67	
Total		100.00		100.00	

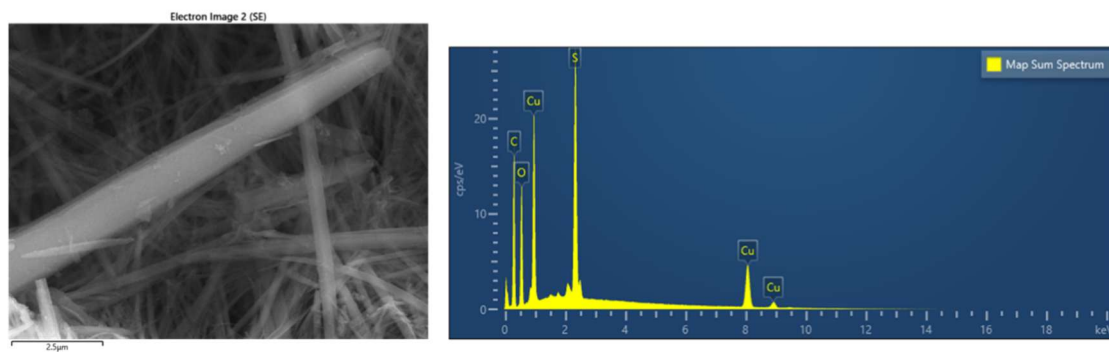


Fig. S6. The elemental mapping of CuMOF-1D.

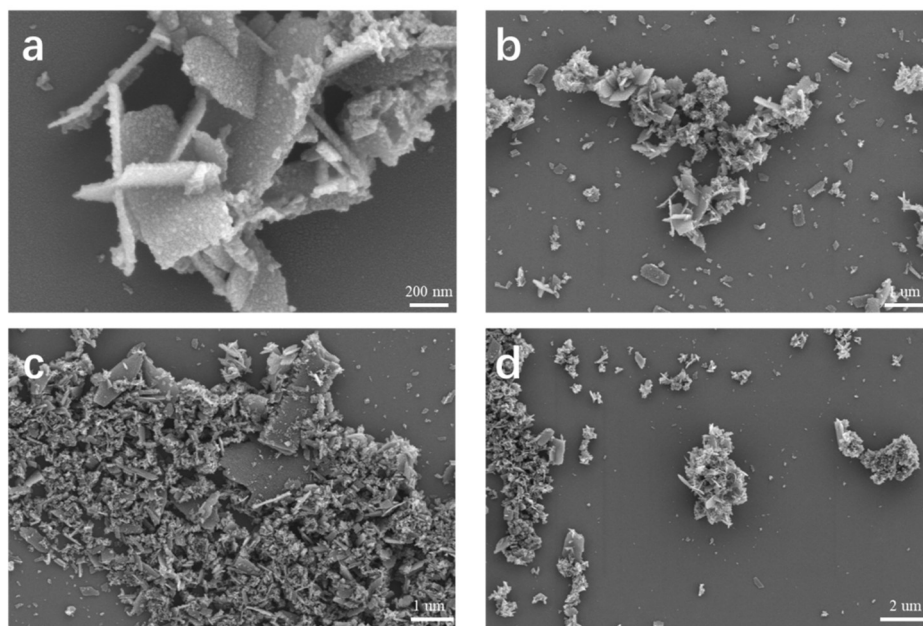


Fig. S7. The SEM images of *sql*-CuMOF-2D.

Map Sum Spectrum					
Element	Line Type	Weight %	Weight % Sigma	Atomic %	
C	K series	61.51	0.43	77.07	
O	K series	18.17	0.35	17.09	
S	K series	4.41	0.10	2.07	
Cu	L series	15.92	0.33	3.77	
Total		100.00		100.00	

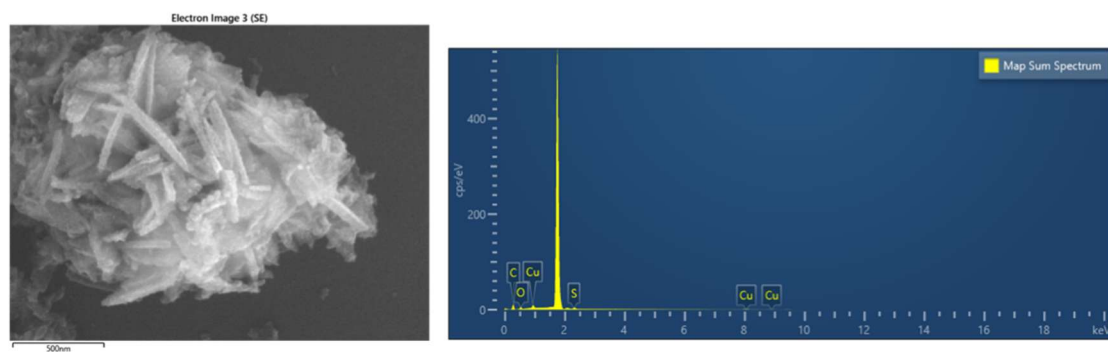


Fig. S8. The elemental mapping of *sql*-CuMOF-2D.

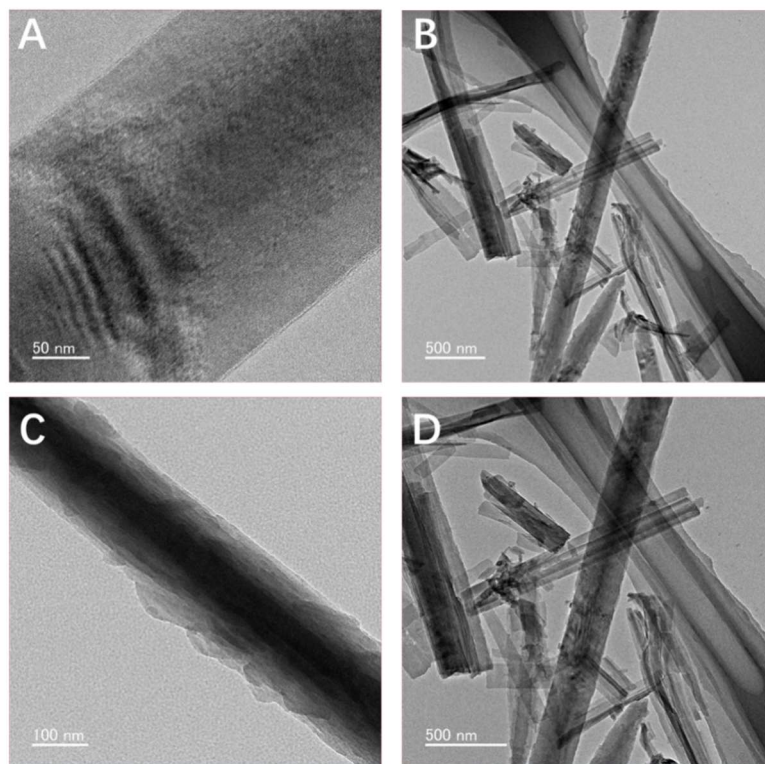


Fig. S9. The HR-TEM images of CuMOF-1D.

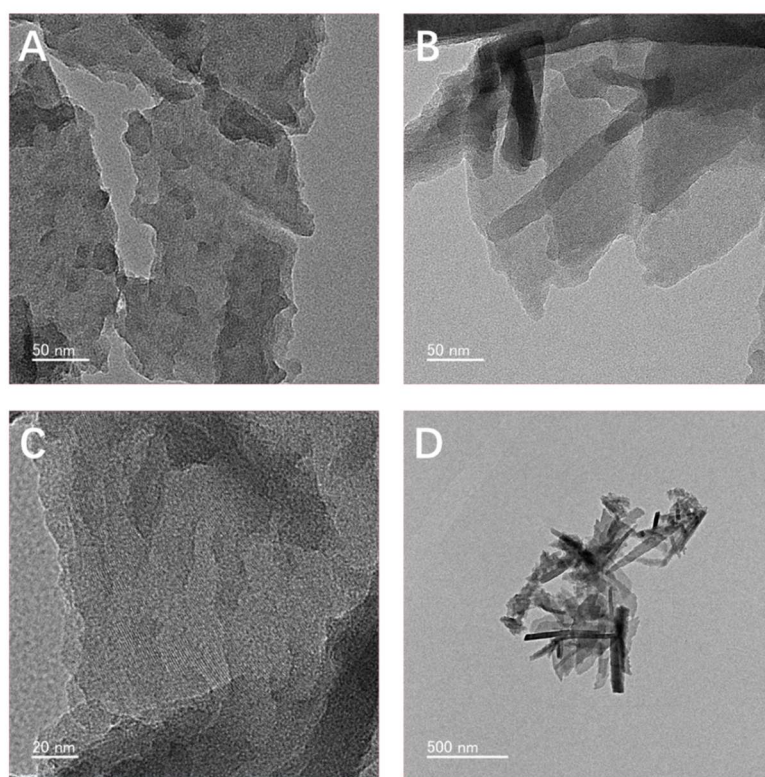


Fig. S10. The HR-TEM images of *sql*-CuMOF-2D.

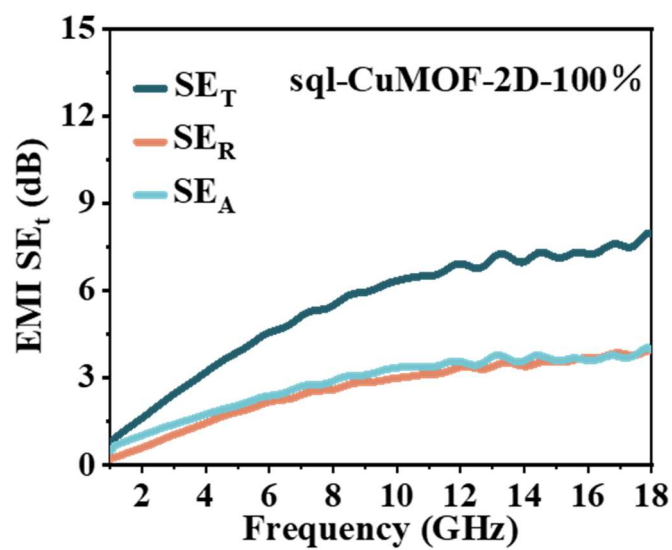


Fig. S11. The EMI SE_T, SE_R and SE_A of *sql*-CuMOF-2D.

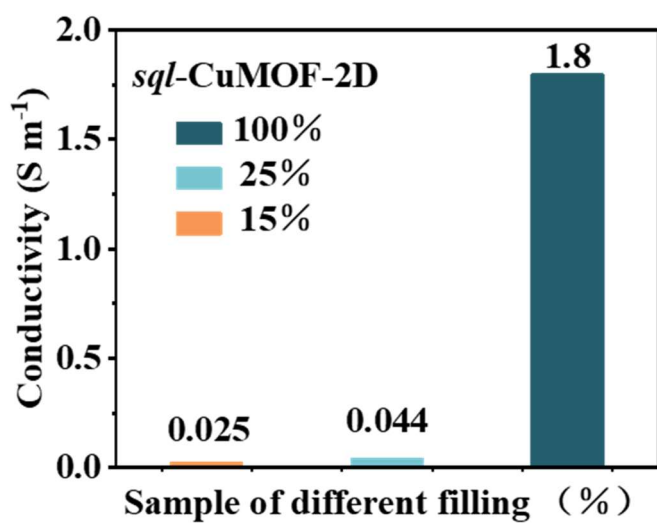


Fig. S12. The conductivity of *sql*-CuMOF-2D with different mass fraction.

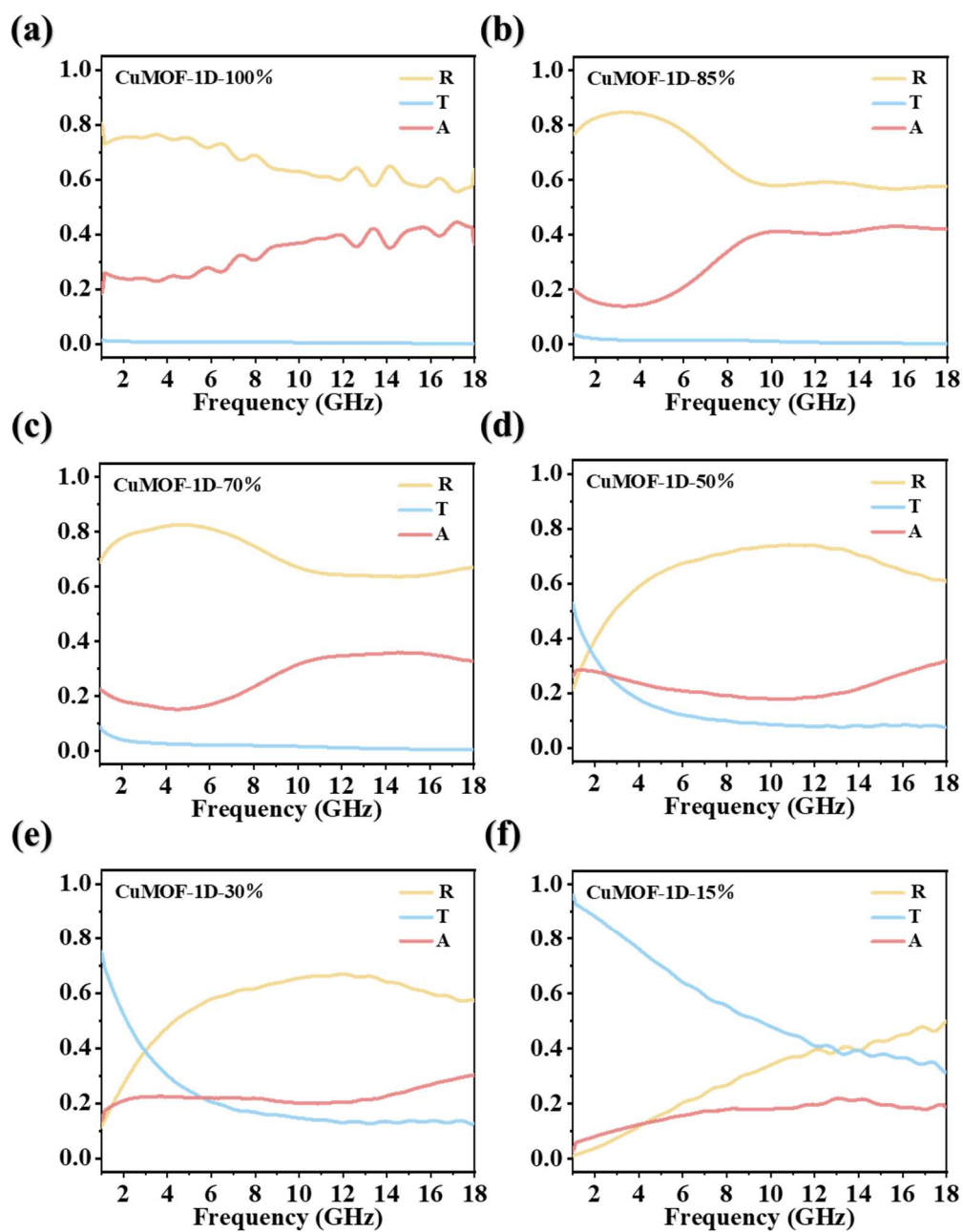


Fig. S13. The reflection coefficient (R), transmission coefficient (T), and absorption coefficient (A) of CuMOF-1D at different electrical conductivity.

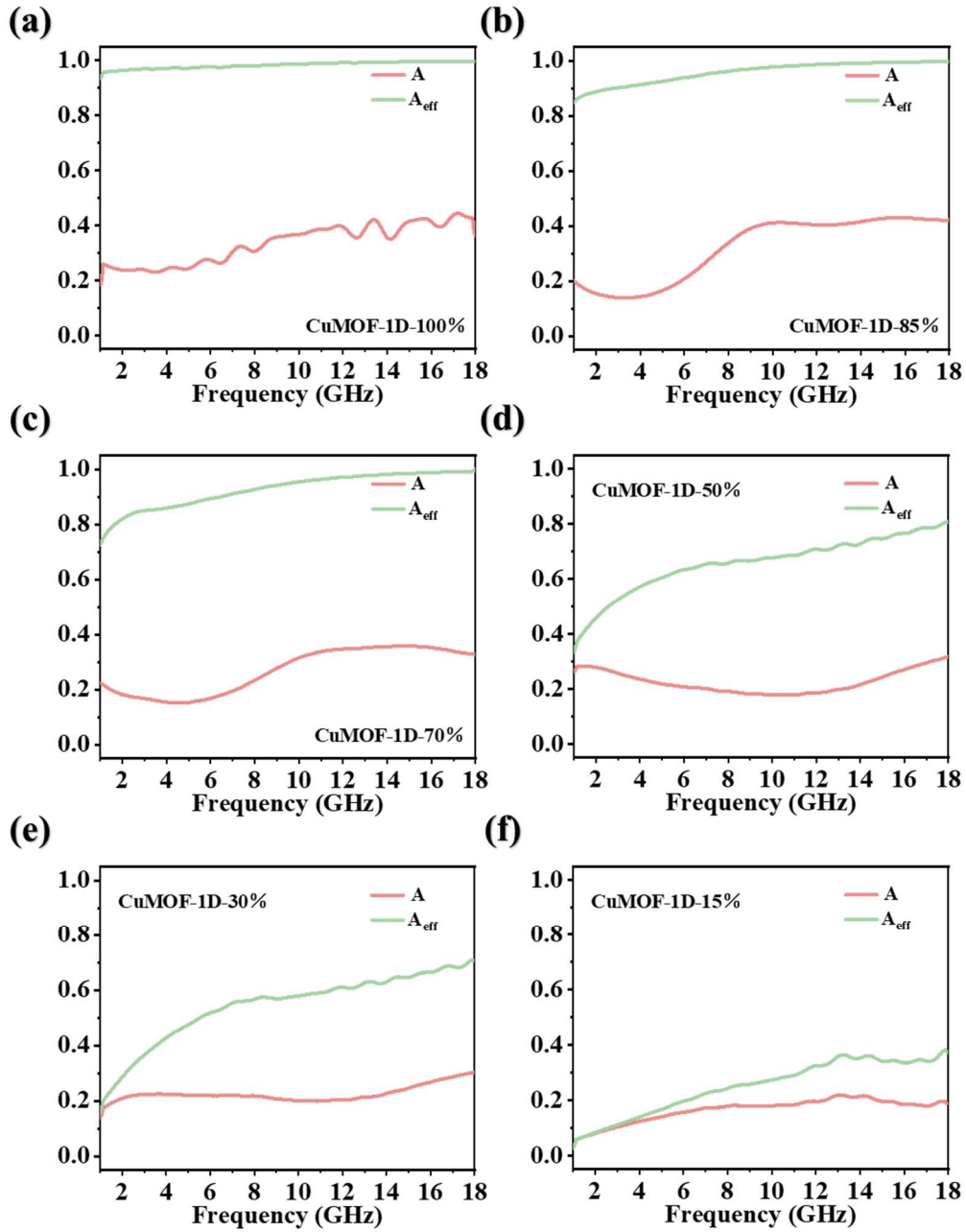


Fig. S14. The absorption coefficient (A) and effective absorption efficiency (A_{eff}) of CuMOF-1D at different electrical conductivity.

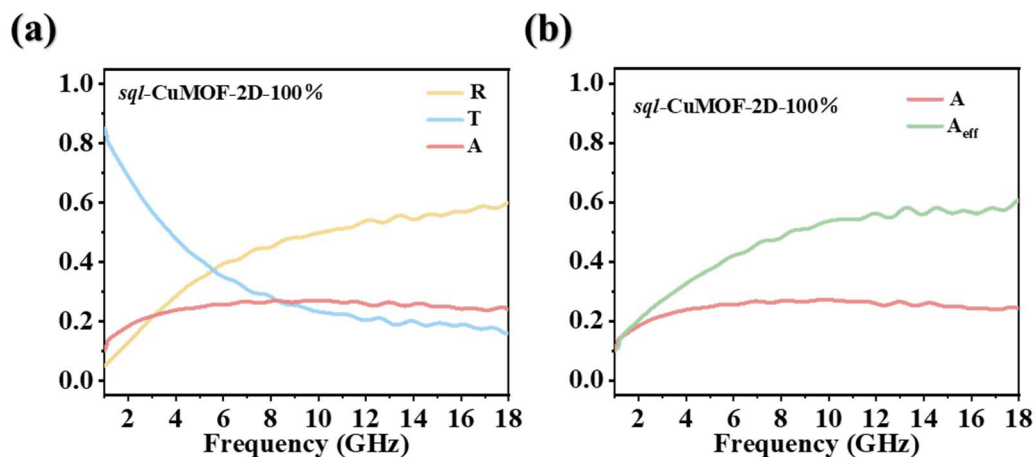


Fig. S15. The reflection coefficient (R), transmission coefficient (T), absorption coefficient (A) and effective absorption efficiency (A_{eff}) of *sql*-CuMOF-2D.

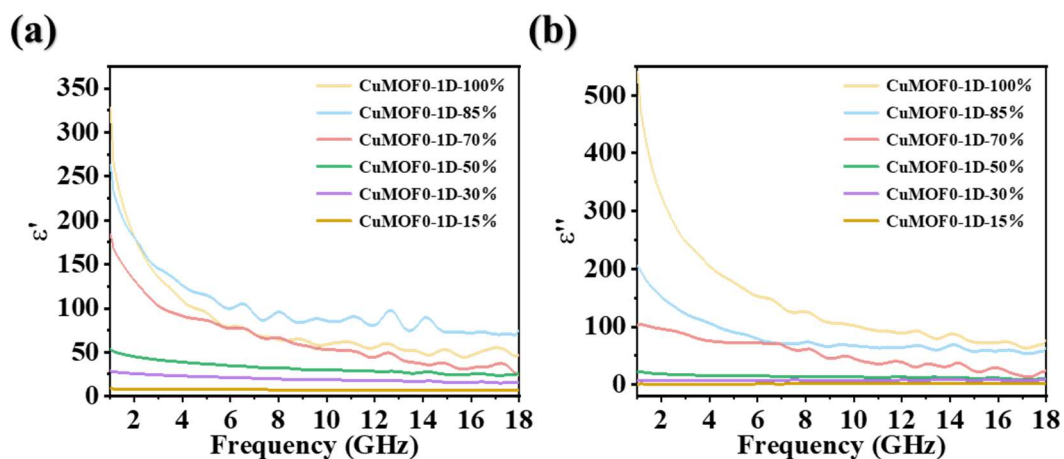


Fig. S16. Real (a) and imaginary (b) parts of the complex dielectric constant of CuMOF-1D at different mass fractions.

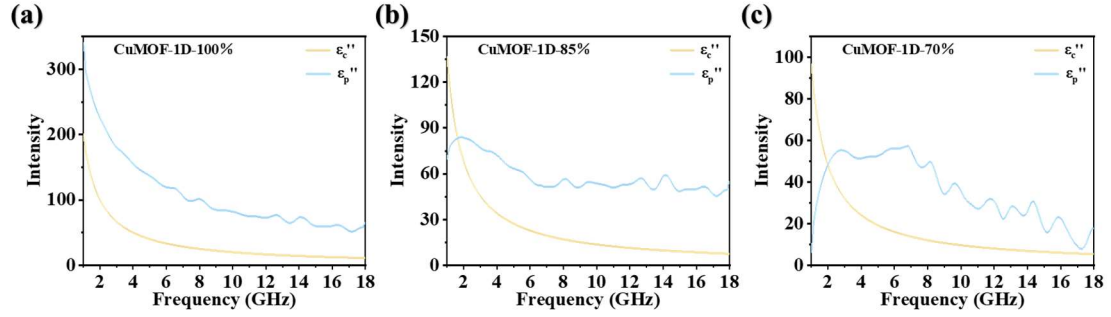


Fig. S17. Contribution values of conduction loss and polarization loss of CuMOF-1D at different mass fractions.

Table S1. Performance comparison between CuMOF-1D and reported electromagnetic wave shielding materials.

Sample	SE _T (dB)	f (GHz)	Thickness (mm)	Ref.
Cellulose fiber/graphene aerogel	47.5	8.2 – 12.4	5.0	[8]
Epoxy/rGO/Ni-chains microcellular foam	25.96	8.2 – 12.4	2.0	[9]
PANI/CNF aerogels	32.0	8.2 – 12.4	5.0	[10]
(CNT)/chitosan	37.6	8.2 – 12.4	2.5	[11]
Polystyrene/MWCNT	23.7	8.2 – 12.4	1.8	[12]
LGA-EP	30.0	8.2 – 12.4	3.0	[13]
GF@PDMS	36.0	8.2 – 12.4	4.5	[14]

Polyurethane/graphene	20.0	12 – 18.0	2.4	[15]
PEDOT/RGO/SrFe ₁₂ O ₁₉	42.2	8.2 – 12.4	2.5	[16]
Fe nanoparticles coated amorphous carbon nanosphere	21.0	8.2 – 12.4	1.2	[17]
f-Ti ₂ CT _x /PVA	28.0	8.2 – 12.4	3.7	[18]
Ordered mesoporous carbon/fused silica	7.5	8.0 – 12.0	5.0	[19]
Polylactic acid/MWCNT	37.0	8.2 – 12.4	5.0	[20]
PMMA/graphene	20.0	8.0 – 12.0	4.0	[21]
CuMOF-1D	34.1	1.0– 18.0	2.0	This work

Reference

- [1] Z. Shan, J. Xiao, M. Wu, *Angew. Chem. Int. Ed.* **63** (2024) e2024016.
- [2] Kresse, G.; Furthmüller, *J. Phys. Rev. B.* **1996**, *54*, 11169–11186.
- [3] Perdew, J. P.; Burke, K.; Ernzerhof, M. Generalized Gradient Approximation Made Simple. *Phys. Rev. Lett.* **1996**, *77*, 3865–3868.
- [4] Kresse, G.; Joubert, D. From Ultrasoft Pseudopotentials to the Projector Augmented-Wave Method. *Phys. Rev. B.* **1999**, *59*, 1758-1775.
- [5] Blöchl, P. E. Projector Augmented-Wave Method. *Phys. Rev. B.* **1994**, *50*, 17953-17979.

- [6] S. Grimme, J. Antony, S. Ehrlich, and S. Krieg, *J. Chem. Phys.* **2010**, *132*, 154104.
- [7] S. Grimme, S. Ehrlich, and L. Goerigk, *J. Comp. Chem.* **2011**, *32*, 1456.
- [8] Y.J. Wan, P.L. Zhu, S.H. Yu, R. Sun, C.P. Wong, W.H. Liao, Ultralight, super-elastic and volume-preserving cellulose fiber/graphene aerogel for high-performance electromagnetic interference shielding, *Carbon* *115* (2017) 629–639.
- [9] Q. Gao, G.C. Zhang, Y. Zhang, X. Fan, Z.W. Wang, S. Zhang, et al., Absorption dominated high-performance electromagnetic interference shielding epoxy/ functionalized reduced graphene oxide/Ni-chains microcellular foam with asymmetric conductive structure, *Compos. Sci. Technol.* *223* (2022), 109419.
- [10] A.R. Pai, T. Binumol, D.A. Gopakumar, D. Pasquini, B. Seantier, N. Kalarikkal, et al., Ultra-fast heat dissipating aerogels derived from polyaniline anchored cellulose nanofibers as sustainable microwave absorbers, *Carbohydr. Polym.* *246* (2020), 116663.
- [11] M.Z. Li, L.C. Jia, X.P. Zhang, D.X. Yan, Q.C. Zhang, Z.M. Li, Robust carbon nanotube foam for efficient electromagnetic interference shielding and microwave absorption, *J. Colloid Interface Sci.* *530* (2018) 113–119.
- [12] J. Chen, X. Liao, W. Xiao, J.M. Yang, Q.Y. Jiang, G.X. Li, Facile and green method to structure ultralow-threshold and lightweight polystyrene/MWCNT composites with segregated conductive networks for

efficient electromagnetic interference shielding, *ACS Sustain. Chem. Eng.* 7 (2019) 9904–9915.

[13] Z. He, J. Sun, L. Zhang, Y. Wang, H. Ren, J. Bao, Synergistic reinforcing and toughening of polydicyclopentadiene nanocomposites with low loadings vinyl-functionalized multi-walled carbon nanotubes. *Polymer* 153 (2018) 287–294.

[14] Z. Zhang, M. Liu, M. Ibrahim, H. Wu, Y. Wu, Y. Li, G. Mersal, I. Azab, S. El-Bahy, M. Huang, Y. Jiang, G. Liang, P. Xie, C. Liu, Flexible polystyrene/graphene composites with epsilon-near-zero properties. *Adv. Compos. Hybrid. Mater.* 5 (2022) 1054–1066.

[15] Y. Li, B. Shen, D. Yi, L.H. Zhang, W.T. Zhai, X.C. Wei, et al., The influence of gradient and sandwich configurations on the electromagnetic interference shielding performance of multilayered thermoplastic polyurethane/graphene composite foams, *Compos. Sci. Technol.* 138 (2017) 209–216.

[16] J. Dalal, S. Lather, A. Gupta, R. Tripathi, A.S. Maan, K. Singh, et al., Reduced graphene oxide functionalized strontium ferrite in poly(3,4-ethylenedioxythiophene) conducting network: a high-performance EMI shielding material, *Adv. Mater. Technol.* 4 (2019), 1900023.

[17] Z.R. Jia, K.C. Kou, S. Yin, A.L. Feng, C.H. Zhang, X.H. Liu, et al., Magnetic Fe nanoparticle to decorate N dotted C as an exceptionally absorption-dominate electromagnetic shielding material, *Compos. B Eng.*

189 (2020), 107895.

[18] J. Liu, Y. Liu, H. Zhang, Y. Dai, Z. Liu, Z. Yu, Superelastic and multifunctional graphene-based aerogels by interfacial reinforcement with graphitized carbon at high temperatures. *Carbon* 132 (2018) 95–103.

[19] J.C. Wang, C.S. Xiang, Q. Liu, Y.B. Pan, J.K. Guo, Ordered mesoporous carbon/ fused silica composites, *Adv. Funct. Mater.* 18 (2008) 2995–3002.

[20] G.L. Wang, L. Wang, L.H. Mark, V. Shaayegan, G.Z. Wang, H.P. Li, et al., Ultralow-threshold and lightweight biodegradable porous PLA/MWCNT with segregated conductive networks for high-performance thermal insulation and electromagnetic interference shielding applications, *ACS Appl. Mater. Interfaces* 10 (2018) 1195–1203.

[21] H.B. Zhang, Q. Yan, W.G. Zheng, Z.X. He, Z.Z. Yu, Tough graphene-polymer microcellular foams for electromagnetic interference shielding, *ACS Appl. Mater. Interfaces* 3 (2011) 918–924.